Novel multiferroic $Bi_2Fe_4O_9$ nanoparticles: the interesting optical, photocatalytic, and multiferroic properties

X. H. WU[a], J. MIAO[a*], Y. ZHAO[a], X. B. MENG[a], X .G. XU[a], S. G. WANG[b], Y. JIANG[a]
[a]*School of Materials Science and Engineering, University of Science and Technology Beijing, Beijing 100083, China*
[b]*State Key Laboratory of Magnetism, Institute of Physics, Chinese Academy of Sciences, Beijing 100190, People's Republic of China*

The single-crystalline multiferroic $Bi_2Fe_4O_9$ nanoparticle has been synthesized using glycine combustion method. The size of the $Bi_2Fe_4O_9$ particle increases from 50 nm to 800 nm with increasing annealing temperature from 923 K to 1173 K. The microstructures of $Bi_2Fe_4O_9$ nanocrystal were observed from transmission electron microscopy and selected area electron diffraction. Moreover, with increasing annealing temperature, the photocatalysis properties of $Bi_2Fe_4O_9$ nanoparticles were greatly improved. The degradation rate of the methyl_orange solution of $Bi_2Fe_4O_9$ nanoparticles was higher as 98%. The resistive switching properties of $Bi_2Fe_4O_9$ nanoparticles were investigated via current-voltage measurements. Interestingly, a bistable resistive switching characteristic was achieved at ambient temperature, which exhibits a potential for next generation nonvolatile memory applications.

(Received July 20, 2012; accepted February 20, 2013)

Keywords: $Bi_2Fe_4O_9$ nanoparticles, Multiferroic, Photocatalysis, Resistive switching

1. Introduction

Multiferroic, which emerge ferromagnetic, ferroelectric, and ferroelastic simultaneously, has attracted much attentions due to the potential applications in sensor, transducers, magnetic recording, and spintronics [1]. Enormous of investigations were conducted on the structural and physical properties of $BiFeO_3$ materials [2-3]. However, few reports were focused on the non-stoichiometric $BiFeO_3$ materials [4-5]. Among that, multiferroic $Bi_2Fe_4O_9$ exhibits great interesting due to its special electric properties, magnetic, catalytic and other properties [6]. The transition from paramagnetism to antiferromagnetism in $Bi_2Fe_4O_9$ with Pbam space-group occurs at a Neel temperature of T_N≈240-265 K [7-8]. In addition, due to the high sensitivity to ethanol and acetone vapors, $Bi_2Fe_4O_9$ can be adopted in manufacture of semiconductor gas sensors, and be employed as industrial ammonia oxidation to NO catalyst [9]. More interesting, an excellent photoresponses in the visible range of $Bi_2Fe_4O_9$ can be observed. Moreover, in the field of photocatalytic, $Bi_2Fe_4O_9$ exhibited enhanced photodegration rate of MO [10-11].

However, to our knowledge, there is no report of $Bi_2Fe_4O_9$ nanoparticles prepared by glycine combustion method until now. The single-crystalline $Bi_2Fe_4O_9$ nanoparticles exhibit a weak ferromagnetism at lower annealing temperature and a relative larger coercivity in small magnetic field. Surprisingly, photocatalysis of the degradation rate of $Bi_2Fe_4O_9$ nanoparticles was found as high as more than 90%. Moreover, an interesting resistive switching characteristic was found in $Bi_2Fe_4O_9$ nanoparticles, which may due to the fuse/refuse filaments composed of oxygen vacancies during the electrical process.

2. Experimental procedures

$Bi_2Fe_4O_9$ nanoparticles were synthesized by glycine combustion method. All the chemical solutions are analytic grade reagents with high purity. Bismuth nitrate $[Bi(NO_3)_3{\cdot}5H_2O]$ and iron nitrate $[Fe(NO_3)_3{\cdot}9H_2O]$ in stoichiometric compositions with a molar ratio of 1:2 were dissolved in nitric acid with stirring. Aminoacetic acid $[C_2H_5NO_2]$ was added to the solution for its accelerating dissolve and followed by heating to 150 ^{0}C in intelligent magnetic stirrer for synthesizing nanoparticle. The nanoparticles were annealed at various temperatures ranging from 650 ^{0}C to 900 ^{0}C for 2 hours, respectively.

The crystal structure, size and micrographs of the samples were investigated by X-ray diffraction (XRD), field emission scanning electron microscopy (SEM) and transmission electron microscopy (TEM). Magnetic measurements were performed on a physical property measurement system (PPMS, Quantum Design). The UV-vis absorption spectra were measured on a UV-vis spectrophotometer. The bistable resistive switching characteristic was achieved in current-voltage measurements at ambient temperature. Ferroelectric hysteresis loops were measured by radiant precision LC test system. I-V characteristics of the samples were measured through a Keithley electrometer.

The photocatalytic activity of $Bi_2Fe_4O_9$ nanoparticles was examined under irradiation of a 500 W iodine-tungsten lamp, and the distance of between the lamp and

the stirrer was 0.5 meter. The initial concentration of methyl orange was 20 mg/L with a catalyst loading of 2 g/L. The catalyst and 100 mL methyl solution were mixed in a beaker. Initially the mixed solutions were stirred in the dark situation for 20 minutes to reach the adsorption equilibrium for preparing the sampling solution, and followed by irradiating process. The solution was sampled every 30 minutes and centrifuged. The concentration of methyl orange was examined by photoabsorption at 465 nm using a UV-vis spectrophotometer. The absorbance was converted to the methyl orange concentration based on a standard curve, and it displayed a linear behavior between the concentration and the absorbance at 465 nm.

3. Results and discussion

The crystallinity of the $Bi_2Fe_4O_9$ nanoparticles was examined with XRD. Fig. 1 shows XRD patterns of the samples prepared at different annealing temperatures. According to the Bi_2O_3-Fe_2O_3 phase diagram [12], the annealing temperature was chosen from 450 ^{0}C to 900 ^{0}C. It is evident that at 450 ^{0}C, the main composition is $BiFe0_3$ co-existing with a small amount of $Bi_{25}FeO_{40}$ and $Bi_2Fe_4O_9$. At 550 ^{0}C, $Bi_{25}FeO_{40}$ completely disappeared, while the peaks of $Bi_2Fe_4O_9$ phase became more obvious. With increasing annealing temperature, the phase of $BiFeO_3$ tends to decline and the content of $Bi_2Fe_4O_9$ increases. The single phase of $Bi_2Fe_4O_9$ is observed at 650 ^{0}C since diffraction peaks fit well to the orthorhombic $Bi_2Fe_4O_9$ (JCPDS: -0090) with a space group of Pbam. The lattice parameters of the $Bi_2Fe_4O_9$ sample prepared at 650 ^{0}C are a=0.7965 nm, b=0.8440 nm, and c=0.5994 nm. In addition, with increasing the annealing temperature, the intensities of the diffraction peaks enhance, indicating a better crystallization and grain growth.

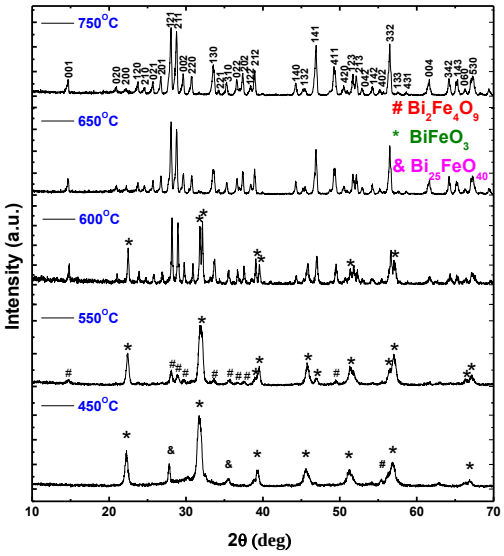

Fig. 1. XRD patterns of the samples prepared in various annealing temperatures.

Fig. 2 shows the morphologies of the $Bi_2Fe_4O_9$ nanoparticles synthesized at the various annealing temperatures at, (a) 650 ^{0}C, (b) at 750 ^{0}C, (c) at 850 ^{0}C, and (d) 900 ^{0}C, respectively. It shows that the shape of $Bi_2Fe_4O_9$ nanoparticles transforms gradually from square to sphere, with increasing annealing temperature. Comparing with $Bi_2Fe_4O_9$ nanosheets prepared by hydrothermal method [13], our $Bi_2Fe_4O_9$ nanoparticles exhibits laminar, cuboid and flower-liked shapes which may due to the different concentrations of NaOH solutions. Based on the SEM, it can be seen that the grains size becomes higher with increasing annealing temperature. Moreover, the size of the $Bi_2Fe_4O_9$ nanoparticles was strongly dependent on annealing temperature. The average grain sizes are approximately 50 nm, 300 nm, 750 nm and 800 nm corresponding to the samples annealed at 650 ^{0}C, 750 ^{0}C, 850 ^{0}C, and 900 ^{0}C.

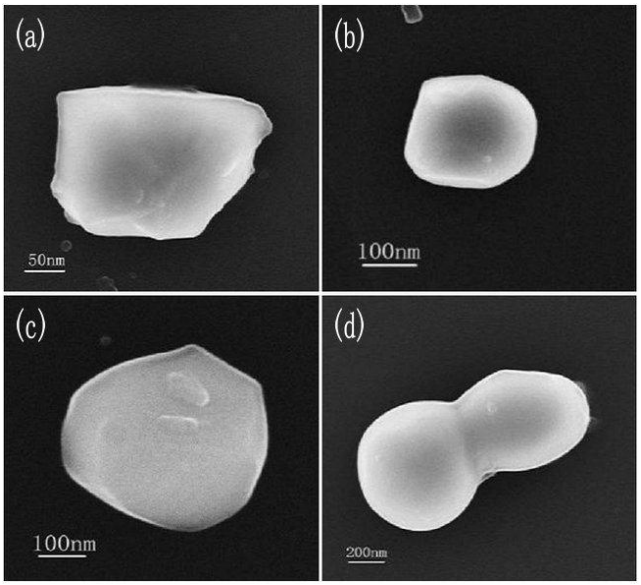

Fig. 2. The SEM micrographs for $Bi_2Fe_4O_9$ nanoparticles annealed at: (a) 650 ℃, (b)750 ℃, (c) 850 ℃, and (d) 900 ℃.

The microstructure and growth orientation of $Bi_2Fe_4O_9$ crystals have been further investigated by TEM. Fig. 3 (a) shows a typical TEM of $Bi_2Fe_4O_9$ sample synthesized at 650 ^{0}C. It might be regarded as the crystal anisotropy induced by the strain's bending planar sheets [14]. The SAED of an individual particle show some sharp diffraction spots, indicating the formation of well-developed, single-crystalline $Bi_2Fe_4O_9$ (Fig 3 (b)). The reflections belong to the (200) and (001) crystal zone, and in different areas have the same growth orientation. In order to confirm the single-crystalline nature of the structure, a HRTEM image obtained from a part of the particle is displayed in Fig 3(b). The regular planar distance are approximately 0.5924 nm and 0.3984 nm, which correspond to (001) and (200) planes of the orthorhombic $Bi_2Fe_4O_9$. This demonstrates that the particles are well crystallized with a single phase structure. Following chemical elements were detected: Bi, Fe and O.

C element is also observed which may be originated from carbon injection process.

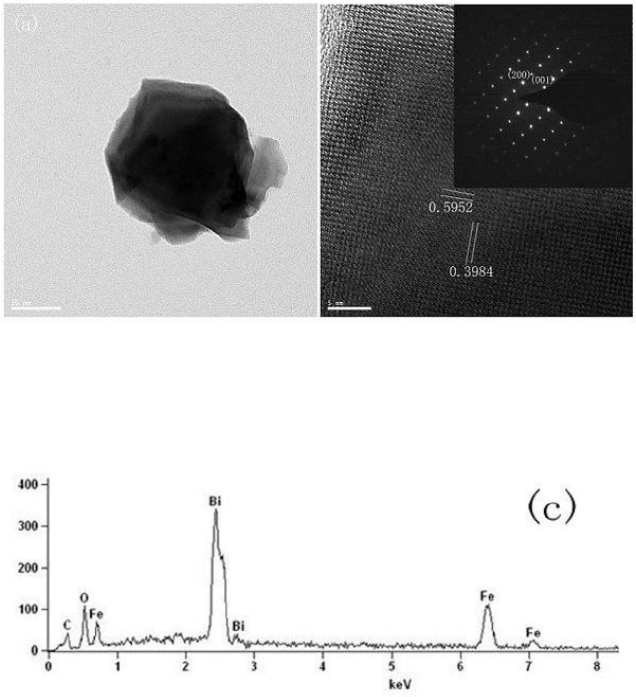

Fig. 3. HRTEM and SAED pattern of the $Bi_2Fe_4O_9$ sample prepared at 650 ℃. The inset is the diffraction spot of this $Bi_2Fe_4O_9$ sample.

Fig. 4 shows the magnetization hysteresis loops of $Bi_2Fe_4O_9$ nanoparticles at a ambient temperature. The sample prepared at 650 ^{0}C shows weak ferromagnetic behavior with a coercivity H_C of 74 Oe, a saturation moment M_S of 0.0814 emu/g and a remnant magnetization Mr of 0.0132 emu/g. Moreover, the saturation magnetic moments for the other samples at various annealing temperature are 0.0351 emu/g at 750 ^{0}C and 0.0266 emu/g at 850 ^{0}C, respectively. $Bi_2Fe_4O_9$ crystals, which are prepared by hydrothermal method and ethylene diamine tetraacetic acid (EDTA) precursor route at 650 ^{0}C, exhibit paramagnetic characteristics and weak ferromagnetic behavior with coercivity Hc of 105 Oe [15-16]. Magnetic hysteresis loops as shown in Fig. 4 indicate that the saturation magnetic moments decrease with increasing temperature from 650 ^{0}C to 850 ^{0}C, it caused the formation of paramagnetic phase. The XRD analysis reveals that there was no evidence of other ferromagnetic impurities. Thus the ferromagnetic behavior should be originated from $Bi_2Fe_4O_9$ nanoparticle. Recently, a surface layer with non-collinear spins has been observed in some oxides such as $NiFe_2O_4$, CoFe2O4 [17-18]. Based on these reports, the structure of our $Bi_2Fe_4O_9$ multiferroic particles can be regarded as a core-shell magnetic structure, and the inner part forms antiferromagnetic ordered structure while the surface forms ferromagnetic ordered structure.

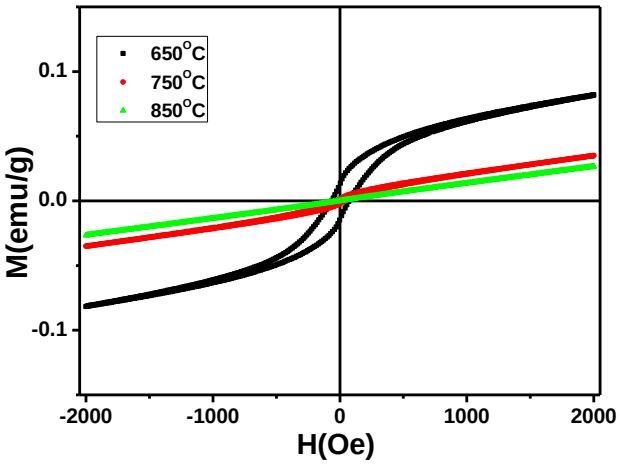

Fig. 4. Magnetic hysteresis loops at room temperature for $Bi_2Fe_4O_9$ samples prepared in various annealed temperature.

Before studying the visible catalytic properties of $Bi_2Fe_4O_9$ nanoparticles with various grain sizes, UV-vis diffuse reflectance spectra of the sample is measured. As shown in Fig 5(a), the absorption edge of $Bi_2Fe_4O_9$ particles is in the visible range of 410-610 nm, indicating that the material can absorb visible light in this wavelength range [13]. Fig. 5(b) shows the forbidden band gap of the $Bi_2Fe_4O_9$ is 1.9 eV, which is estimated from tangent line in a plot of the square root of Kubelka-Munk function F(R) against photo energy [19]. The band gap is smaller than that of prepared hydrothermal method (2.1 eV) [20], indicating that $Bi_2Fe_4O_9$ has possibility of utilizing more visible light for photocatalytic. Fig. 5(c) shows the photocatalytic activities of all samples in temperature ranging from 650 ^{0}C to 900 ^{0}C. The efficiencies are varying from 98% to 93%. Firstly, the catalytic activity of $Bi_2Fe_4O_9$ is significantly affected by its specific surface area [21]. Generally, the smaller the particle size is, the larger the specific surface area is. Secondly, since a photocatalytic reaction should occur at interface between catalyst surface and reagents, the electron-hole pairs on catalyst surfaces are related to the photocatalytic reaction [22]. In the case of large size, the hopping from inner to the surface of $Bi_2Fe_4O_9$ nanoparticles for the electron-hole pairs takes a long time. Moreover, the electron-hole recombination of $Bi_2Fe_4O_9$ nanoparticles is expected to occur during the electron-hole diffusing, leading to the lower photocatalytic efficiency for larger particles.

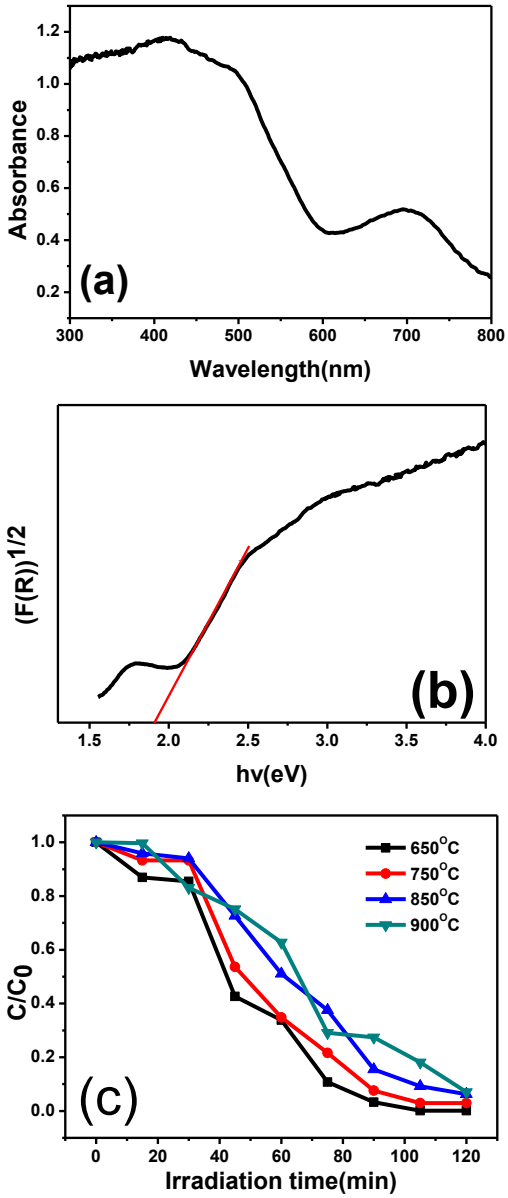

Fig. 5. (a) UV-vis diffuse reflectance spectra of $Bi_2Fe_4O_9$ nanoparticles prepared at 750℃; 5(b) F(R)1/2-hv curves, where the short dotted line is tangent of the linear part and 5(c) photocatalytic of $Bi_2Fe_4O_9$ nanoparticles with different grain sizes on degradation of methyl orange.

Fig. 6 shows the interesting resistive switching properties of $Bi_2Fe_4O_9$ nanoparticles. As well known, the filaments composed of oxygen vacancies presented in $Bi_2Fe_4O_9$ nanoparticles may fuse/refuse under the same voltage polarity. During forming process with applying a positive bias voltage in the bottom electrode (BE), oxygen vacancies in $Bi_2Fe_4O_9$ nanoparticles are aligned to form a conduction path due to a high electric field. With applying a positive bias voltage on the top electrode (TE), the oxygen ions are aligned along the reversal way in $Bi_2Fe_4O_9$ nanoparticles. With a large current flowing through the conduction path, the Joule heating and dispersion of oxygen vacancies driving a low resistance state (LRS) converted to a high resistance state (HRS). With changing the direction of the applied voltage, the oxygen ions went to the $Bi_2Fe_4O_9$ nanoparticles layer and the conduction path rebuilt again.

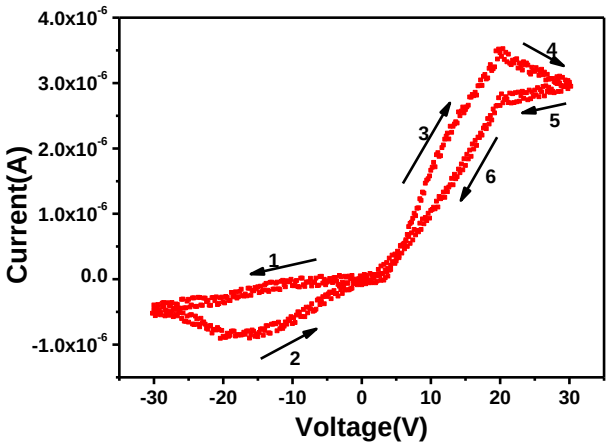

Fig. 6. A typical I-V characteristic of $Bi_2Fe_4O_9$ nanoparticles.

4. Conclusions

Single-crystalline $Bi_2Fe_4O_9$ nanoparticles with various grain sizes have been successfully synthesized by glycine combustion method. As the annealing temperature increasing, the grain sizes, of which the grains grow along (001) and (200) directions, gradually increase from 50 to 800 nm. The magnetic properties of the samples are strongly depended on the grain size. As the size increasing, the saturation magnetization and the degradation rate of the methyl orange solution gradually decrease, and moreover, the weak ferromagnetic behavior transforms into paramagnetic behavior. The forbidden band gap of $Bi_2Fe_4O_9$ nanoparticles are in the visible range, and its numerical value is 1.9 eV. The resistive switching properties of $Bi_2Fe_4O_9$ nanoparticles were investigated in this study. The compliance current influences the set current, set voltage, reset current and reset voltage. Such $Bi_2Fe_4O_9$ multiferroic nanoparticles can be expected to be utilized for next generation nonvolatile memory application.

Acknowledgements

This work was supported by National Basic Research Program of China (No. 2012CB932702), the Beijing Municipal Natural Science Foundation (No. 2122037), the NSFC (Nos. 51071022, 11174031), Fok Ying-Tong Education Foundation (No. 121046), PCSIRT, and the Fundamental Research Funds for the Central Universities.

References

[1] J. Wang, J. B. Neaton, H. Zheng, V. Nagarajan, S. B. Ogale, B. Liu, D. Viehland, V. Vaithyanathan, D. G. Schlom, U. V. Waghmare, N. A. Spaldin, K. M. Rabe, M. Wuttig, R. Ramesh, Science, **299**, 1719 (2003).
[2] J. Miao, X. Zhang, Q. Zhan, Y. Jiang, K. H. Chew, Applied Physics Letters, **99**, 062905 (2011).
[3] J. Miao, B. P. Zhang, K. H. Chew, Y. Wang, Applied Physics Letters, **92**, 062902 (2008).
[4] Z. M. Tian, Y. Qiu, S. L. Yuan, M. S. Wu, Journal of Applied Physics, **108**, 064110 (2010).
[5] Y. Wang, X. Duan, Y. Cui, Nano Letters, **2**, 101 (2002).
[6] Z. W. Yu, H. Y. Miao, G. Q. Tan, Chinese Journal of Organic Chemistry, **24**, 483 (2008).
[7] Z. Yang, Y. Huang, B. Dong, H. L. Li, S. Q. Shi, Journal of Solid State Chemistry, **179**, 3324 (2006).
[8] Y. A. Park, K. M. Song, K. D. Lee, C. J. Won, N. Hur, Applied Physics Letters, **96**, 092506 (2010).
[9] N. I. Zakharchenko, Kinetic Catalysis Letters, **43**, 95 (2002).
[10] J. Kim, C. W. Lee, W. Choi, Environmental Science and Technology, **44**, 6849 (2010).
[11] M. Tabota, K. Maeda, M. Higashi, D. L. Lu, T. Takrta, Langmuir. **26**, 9161 (2010).
[12] R. Palai, R. S. Katiyar, H. Schmid, Physical Review B, **77**, 014110 (2008).
[13] Q. J. Ruan, W. D. Zhang, Journal of Physical Chemistry C, **113**, 4168 (2009).
[14] Z. W. Pan, Z. R. Dai, Z. L. Wang, Science, **291**, 1947 (2001).
[15] Y. G. Wang, G. Xu, Y. Y. Yang, Z. H. Ren, Ceramics International, **35**, 51 (2009).
[16] J. Y. Zhao, T. Liu, Y. B. Xu, Y. Y. He, W. P. Chen, Materials Chemistry and Physics, **128**, 388 (2011).
[17] H. Bi, S. D. Li, Y. C. Zhang, Y. W. Du, Journal of Magnetism and Magnetic Materials, **277**, 363 (2004).
[18] A. E. Berkowitz, J. A. Lahut, I. S. Jacobs, Physical Review Letters, **34**, 594 (1975).
[19] Y. I. Kim, S. J. Atherton, E. S. Brigham, Journal of Physical Chemistry, **97**, 45 (1993).
[20] D. R. Deng, D. Du, S. W. Yu, J. R. Cheng, Procedia Engineering, **27**, 577 (2012).
[21] A. T. Bell, Science, **299**, 1688 (2003).
[22] M. R. Hoffmann, S. T. Martin, W. Y. Choi, D. W. Bahnemann, Chemical Reviews, **95**, 69 (1995).

*Corresponding author: j.miao@ustb.edu.cn